Photoacoustics 31 (2023) 100521

Contents lists available at ScienceDirect

Photoacoustics

journal homepage: www.elsevier.com/locate/pacs

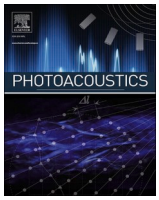

Full-view LED-based optoacoustic tomography

Xiang Liu [a,b,1], Sandeep Kumar Kalva [a,b,*,1], Berkan Lafci [a,b], Daniil Nozdriukhin [a,b], Xosé Luís Deán-Ben [a,b], Daniel Razansky [a,b,*]

[a] Institute of Pharmacology and Toxicology and Institute for Biomedical Engineering, Faculty of Medicine, University of Zurich, Zurich CH-8057, Switzerland
[b] Institute for Biomedical Engineering, Department of Information Technology and Electrical Engineering, ETH Zurich, Zurich CH-8093, Switzerland

ARTICLE INFO

Keywords:
Light emitting diode
Optoacoustic/photoacoustic tomography
Low-cost light sources
Laser

ABSTRACT

Optoacoustic tomography is commonly performed with bulky and expensive short-pulsed solid-state lasers providing high per-pulse energies in the millijoule range. Light emitting diodes (LEDs) represent a cost-effective and portable alternative for optoacoustic signal excitation that can additionally provide excellent pulse-to-pulse stability. Herein, we introduce a full-view LED-based optoacoustic tomography (FLOAT) system for deep tissue in vivo imaging. It is based on a custom-made electronic unit driving a stacked array of LEDs, which attains 100 ns pulse width and highly stable (0.62 % standard deviation) total per-pulse energy of 0.48 mJ. The illumination source is integrated into a circular array of cylindrically-focused ultrasound detection elements to result in a full-view tomographic configuration, which plays a critical role in circumventing limited-view effects, enhancing the effective field-of-view and image quality for cross-sectional (2D) imaging. We characterized the FLOAT performance in terms of pulse width, power stability, excitation light distribution, signal-to-noise and penetration depth. FLOAT of the human finger revealed a comparable imaging performance to that achieved with the standard pulsed Nd:YAG laser. It is anticipated that this compact, affordable and versatile illumination technology will facilitate optoacoustic imaging developments in resource-limited settings for biological and clinical applications.

1. Introduction

The availability of commercial optoacoustic tomography (OAT) systems based on tunable pulsed lasers has led to an explosive growth of the use of this modality in a myriad of biological applications [1–3]. Recently, hand-held systems have also been used in a number of clinical trials further demonstrating the powerful capabilities of this imaging technology for diagnosis of medically-relevant conditions [4–6]. The optical-absorption-based contrast of OAT provides unique advantages for resolving spectrally-distinctive functional contrast from tissue chromophores [7,8], retrieving molecular information from targeted and genetically-encoded agents [9–12], sensing local temperature changes [13–15], as well as high-resolution imaging of rapid biological dynamics [16–22]. However, the use of OAT by biomedical researchers and physicians is largely hampered by the bulky and costly solutions associated with conventional nanosecond laser pulsing technologies. Hence, development of more affordable light sources capable of efficient optoacoustic signal generation can greatly facilitate dissemination of the OAT technology.

Typically, short-pulsed (< 100 ns) light pulses with sufficient energy are required for OAT of biological tissues at millimeters to centimeter depths. OAT is generally performed with Q-switched Nd:YAG lasers having < 10 ns pulse durations and energies from a few to hundreds of mJ [23]. These are often combined with optical parametric oscillator (OPO) crystals enabling tuning the optical wavelength within visible and near-infrared ranges [24]. The high cost and form factor of these lasers represents an important drawback, exacerbated by thermal and other sources of instability leading to significant pulse energy fluctuations. Recently, alternative light sources such as pulsed laser diodes (PLDs) [22,25,26] and light emitting diodes (LEDs) [27–29] have been explored due to their compact size, low cost and ability to operate at high pulse repetition rates (PRRs) of several kHz [30]. LEDs offer a safe (diverging beam) and cost-effective solution for OAT implementations, particularly in resource-limited and clinical settings. The pulse energies delivered by single LED sources are typically in the range of a few μJ, which is arguably insufficient for OAT. However, stacked arrays of LEDs

* Correspondence to: Institute for Biomedical Engineering, Wolfgang-Pauli-Strasse 27, Zurich CH-8093, Switzerland.
E-mail addresses: sandeep.kalva@uzh.ch (S.K. Kalva), daniel.razansky@uzh.ch (D. Razansky).
[1] Authors contributed equally.

https://doi.org/10.1016/j.pacs.2023.100521
Received 28 April 2023; Received in revised form 30 May 2023; Accepted 6 June 2023
Available online 8 June 2023

can deliver higher pulse energies thus can potentially be used for deep tissue imaging purposes if properly arranged to effectively illuminate the imaged volume [31,32].

Angular aperture and detection bandwidth of the ultrasound detection array are key determining factors of the OAT performance [19,33,34]. To this end, LED-based imaging systems have been implemented with linear-array transducers that are afflicted by limited-view artefacts and poor image quality at depths. This can be overcome by rotating the array around the sample, albeit at the expense of lower temporal resolution and other accompanying motion artifacts [35]. Concave arrays of cylindrically-focused elements have been shown to outperform linear arrays by attaining superior image quality due to an increased angular coverage exploiting the tomographic nature of OAT [36,37]. A full ring configuration is particularly advantageous for cross-sectional imaging as it averts the limited-view artefacts, which has successfully been exploited for imaging human finger joints [38–40]. Also, OAT systems based on full-ring arrays can readily be combined with reflection- and transmission-based ultrasound imaging to additionally retrieve pulse-echo images as well as speed of sound and acoustic attenuation maps [41].

Herein, we developed a full-view LED-based optoacoustic tomography (FLOAT) system that employs a stacked array of LEDs integrated into a circular array transducer configuration. We characterize the FLOAT performance in terms of power stability and penetration depth in a tissue-mimicking phantom and compare it to that achieved with a conventional pulsed Nd:YAG laser source. We further demonstrate the feasibility of in vivo imaging of human finger joints with the system.

2. Materials and methods

2.1. FLOAT system

The schematic of the FLOAT system is shown in Fig. 1a. Stacked arrays of 10 high-power LEDs (SFH4171S, OSRAM, Munich, Germany) emitting at 850 nm wavelength were employed as the excitation light source. In total, 16 LED arrays were used, 8 attached on each side (top and bottom) of the custom-designed circular 80 mm-diameter ultrasound array transducer (Imasonic Sas, Voray, France). The LED arrays were arranged such that a uniform illumination is provided around the circumference of the imaged object. A plexiglass membrane was attached on the inner side of the LED array box to isolate the LED circuit from water while being transparent for light delivery. The LED arrays were operated in a pulsed mode by overdriving them with peak currents of ~ 40 A using a custom-designed driver unit (see details in Section 2.2). The driver was triggered with an external function generator (model 33220A, Agilent, CA, USA) producing 80 ns trigger pulses at 50 Hz frequency. The pulsed current delivered to the LED arrays was controlled using a high voltage power supply (WMX-ASD10003, Wemaxpower technology Co. Ltd., Shenzhen, China). The per-pulse energy for each LED is ~ 3 μJ, as measured with a pyroelectric sensor (J-10MT-10KHZ, Coherent Inc.), which results in a total light energy of 0.48 mJ generated with all the 16 LED arrays (160 individual LEDs).

The circular ultrasound array transducer consists of 512 sensing elements, each having $0.37 \times 15\ mm^2$ area, interelement pitch of 0.47 mm, central frequency of 5 MHz and > 60 % nominal detection bandwidth [36]. All transducer elements were equidistantly distributed on 2 arcs, each covering a 174° angle. All the transducer elements are cylindrically focused in the elevational direction at 38 mm distance. The generated optoacoustic signals were digitized by a custom-made parallel data acquisition unit (DAQ, Falkenstein Mikrosysteme GmBH, Taufkirchen, Germany) at 40 mega samples per second and transferred through a 1 Gb/s Ethernet connection to a PC for storage and further processing. The external pulse generator was also used to trigger the DAQ. Data acquisition is controlled using a PC-based MATLAB (R2020b) interface.

2.2. LED driver design

Each pulsed-current LED driver [42] is driving a separate LED waterproof box containing 4 LED arrays. A SiC-based MOSFET (IMZA65R027M1H, Infineon, Munich, Germany) is used as a switch to generate pulsed current on a single LED driver. Each MOSFET is operated by a MOSFET gate driver (TC4422, Microchip, Chandler, USA). Eight capacitors (0.1 μF, C1812C104KCRACAUTO, KEMET, Fort Lauderdale, FL, USA) were used to store sufficient energy for the pulsed electrical current, and 8 current-sensing resistors (800 mΩ, YAGEO, New Taipei City, Taiwan) were connected in series with these capacitors to measure the pulsed current. Four protection diodes (RS07G-M-08, Vishay, Malvern, USA) were connected in reverse parallel with the series of 20 LEDs to prevent the over voltage damage for the LED series. A 1.8 Ω gate source resistor was used to ensure the fast switching of the MOSFET, and a 10 Ω gate sink resistor was used to reduce ringing oscillation during the switch off. Three bypass capacitors (0.1 μF, 0.1 μF, and 4.7 μF) were used for the MOSFET gate driver TC4422 with two SMC connectors (Amphenol RF, Danbury, USA) for triggering and current monitor connection. A 50 Ω resistor was connected in series to the current monitor SMC connector for impedance matching. For the pulse generation, the 8 energy storage capacitors are charged to 340 V to provide enough voltage to overdrive 20 LEDs connected in series. Once the MOSFET is turned on by the gate driver, the capacitor is being

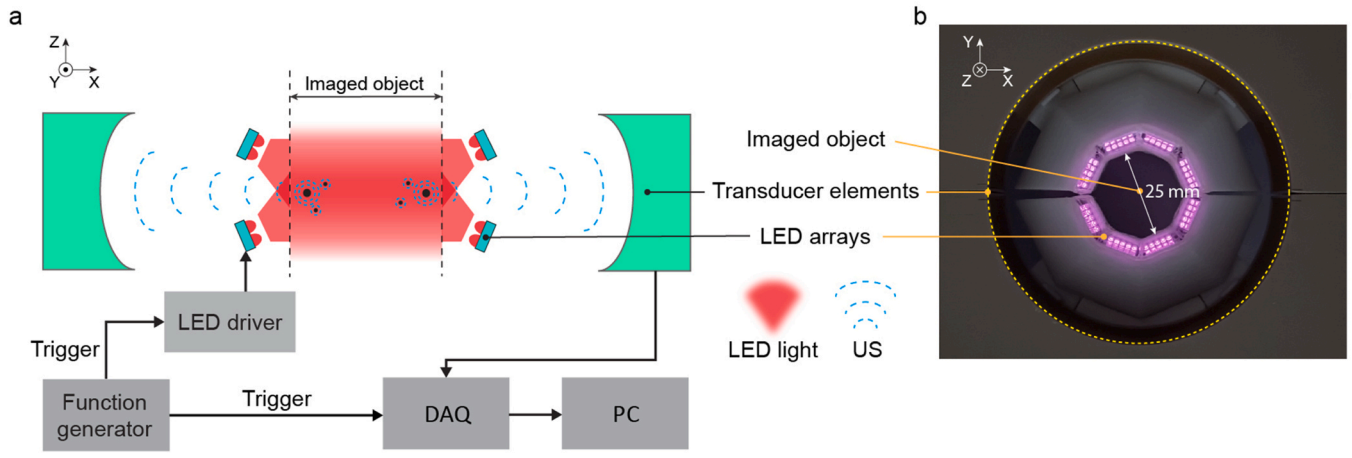

Fig. 1. Full-view LED-based optoacoustic tomography (FLOAT) system for deep tissue in vivo imaging. a, Lay-out of the system. b, Photograph of the LED arrays (only the bottom eight arrays are shown) fixed to the circular-ring array transducer. US: ultrasound.

discharged by the current flowing through the LEDs, causing them to emit light. Subsequently, the falling edge of the trigger signal switches off the pulsed current flowing through the LEDs. The latter can be calculated by measuring, with an oscilloscope, the voltage across the low-side current sensing resistors whose one side is grounded.

2.3. LED array design

Each array consists of 10 LEDs connected in series on a 11 mm long, 5 mm wide aluminum-core based double-layer printed circuit board (PCB). The aluminum core can enhance the heat transfer and cooling down the LEDs. The PCB has two through holes for the positive and negative connection from the back side as well as a customized heatsink glued on the back side of the array using heat transfer glue. The arrays were connected in pairs, yielding a total of 20 individual LED sources connected in each series. Altogether, 8 sets of series-connected LED arrays operated in parallel, corresponding to 160 individual LED sources.

2.4. Signal processing and image reconstruction

Several signal processing steps were implemented prior to the OAT image reconstruction. Initially, the raw optoacoustic signals collected from the imaged object were averaged over multiple consecutive pulses. Next, background noise signals, obtained without the object present in the field of view (FOV), were subtracted and the resultant signals were bandpass-filtered between 0.1 and 8 MHz. A notch filter was then employed to further mitigate strong harmonic noise appearing in the Fourier transform of the signal matrix. The filtered signal matrix was then used for OAT image reconstruction using a model-based reconstruction algorithm featuring statistical weighting to minimize artefacts associated to acoustic reflections and scattering [43].

3. Results

3.1. FLOAT system characterization

Temporal profile of the pulsed current flowing through a LED box, as measured with an oscilloscope (HMO 2024, Rohde&Schwarz, Munich, Germany), is shown in Fig. 2a. The LED light pulse measured by a photodiode (DET10A2, Thorlabs, New Jersey, United States) closely resembles the current pulse shape (Fig. 2a). The full width at half maximum (FWHM) of the light pulse is ~ 100 ns with rise and fall times of ~ 40 ns and ~30 ns, respectively. The normalized pulsed light energy fluctuation is shown in Fig. 2b. The light energy was measured continuously for a duration of 2000 s (~ 33.33 min) at 100 Hz PRR (200 K pulses), resulting in excellent pulse-to-pulse stability (Fig. 2b) with a minor standard deviation of 0.62 %. This constitutes an important asset for dynamic functional and molecular measurements, e.g to map biodistribution of contrast agents or blood sO_2 changes [44]. The light beam profile of the LED arrays was computed using simulations and validated with experimental measurements. For this, TracePro software was employed to simulate the light beam profile generated by the 8 LED arrays occupying one arc (174°) of the transducer array (Fig. 2c). A CMOS camera (BASLER ace 2 Basic) was subsequently used to capture the light beam distribution experimentally (Fig. 2d), exhibiting good correspondence to the simulated results. Considering the total optical energy, this corresponds to a peak energy density of ~ 51 μJ/cm^2 on the surface of the sample.

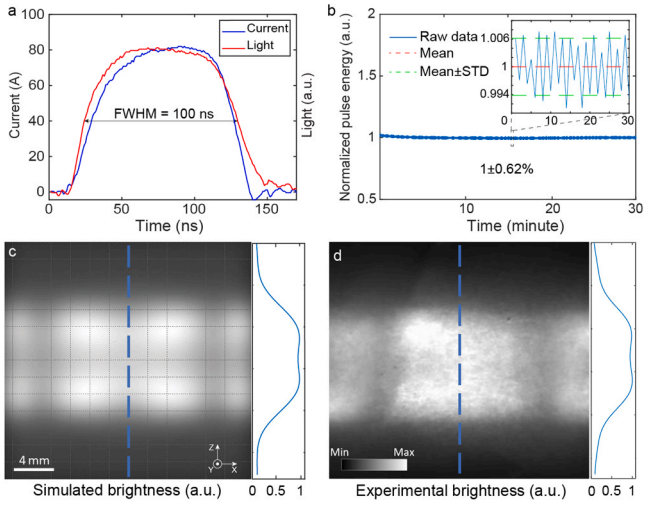

Fig. 2. FLOAT system characterization. a, Pulsed current and light pulse waveform of a LED box. b, LED pulse energy stability over time. Inset shows pulse-to-pulse fluctuations. c and d, Simulated and experimental light beam profiles on the x-z plane with 8 LED arrays corresponding to half of the full-ring ultrasound array transducer and brightness distribution along the dashed lines.

3.2. Imaging performance and comparison with Nd:YAG-based OAT

We compared the FLOAT performance with that of the conventional Nd:YAG laser-based OAT in tissue-mimicking phantoms. Briefly, the excitation laser operated at 850 nm wavelength and 52.8 mJ per pulse energy, resulting in an energy density of 5.9 mJ/cm^2 at the object's surface. The same circular transducer array and DAQ were used for both systems. The imaged phantom consisted of three cylindrical 2 mm diameter black India ink insertions with 2.5 OD optical density, approximately corresponding to whole blood absorption of $\mu_a = 5.7\ cm^{-1}$ at 850 nm [45]. The insertions were embedded at a depth of 3 mm inside a 20 mm agar cylinder (1.3 % agar powder by weight) containing black India ink and 1.2 % by volume of Intralipid to simulate a background absorption coefficient of $\mu_a = 0.23\ cm^{-1}$ and a reduced scattering coefficient of $\mu_s' = 10\ cm^{-1}$ (Fig. 3a). The reconstructed images obtained using laser-based OAT and FLOAT systems for different numbers of averaged frames (1, 10, 100, 1000) are shown in Figs. 3b and 3c, respectively. As expected, all the three ink insertions in the phantom are clearly discernible with the laser-based OAT system, even for single-shot excitation. For FLOAT, the ink insertions are barely visible with less than 10 averages with the image quality consistently increasing with the number of frames being averaged. For a quantitative comparison of FLOAT and laser-based images, the contrast-to-noise-ratio (CNR) as a function of the number of averages is shown in Fig. 3d. The CNR was calculated as $20 * \log_{10}[(Signal - Background)/Noise]$, where *Signal* is the mean signal amplitude in the region of interest (ROI) indicated with a red box (inside ink insertion), *Background* is the mean signal amplitude in the ROI outside the phantom (indicated with a yellow box) and *Noise* is the standard deviation of the noise in the latter ROI. The high CNR for the laser-based images is attributed to the high per-pulse energy with the SNR of the FLOAT images increasing proportionally to the square root of the number of averages. With > 500 averages the FLOAT image quality becomes comparable to that rendered with the laser excitation with all the three ink insertions together with the phantom boundary clearly discernible.

3.3. In vivo human finger imaging

To further demonstrate the potential of the FLOAT system for in vivo imaging, the images of the index finger of a healthy male volunteer were examined and compared with those rendered with the laser-based OAT system. The finger was secured in a 3D-printed plastic holder, which was then fixed within the water tank to minimize any motion during the scan. As a proof-of-concept, the medial phalange of the index finger was scanned, as indicated in Fig. 4a. We then employed a dedicated signal and image processing pipeline to mitigate common artifacts and optimize image quality. While commonly employed filtered back-projection algorithms result in diminished contrast and inadequate representation

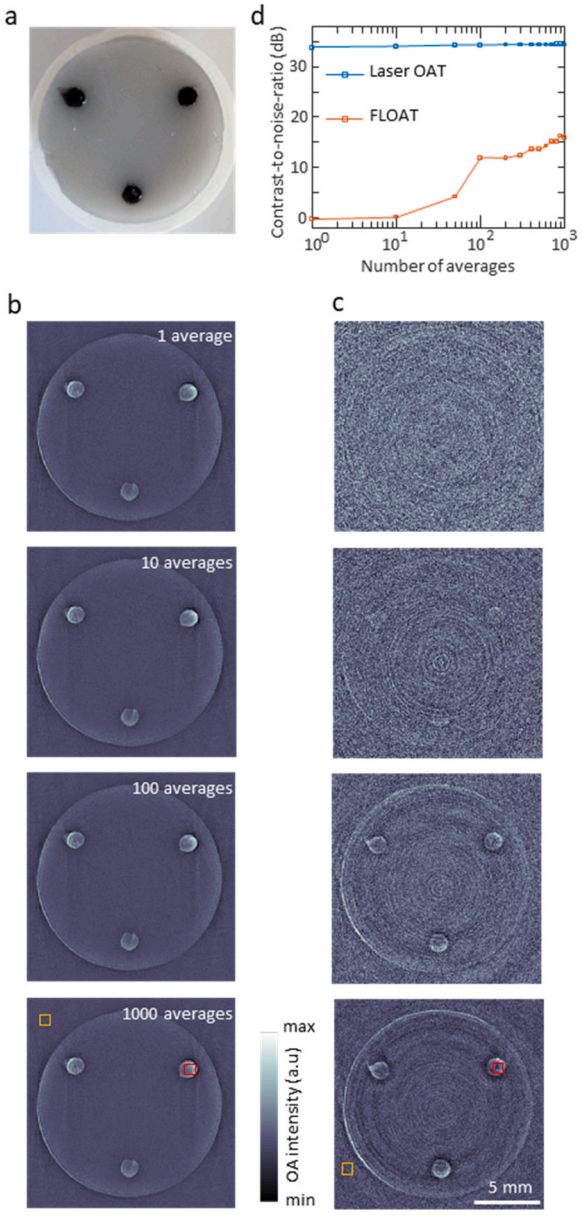

Fig. 3. Performance comparison of FLOAT and Nd:YAG laser-based OAT. a, Photograph of the tissue-mimicking phantom with ink insertions. b and c, Reconstructed OAT images obtained using a Nd:YAG OPO laser (850 nm) and FLOAT, respectively, for different number of consecutive frames (1, 10, 100, 1000) being averaged. d, Contrast-to-noise-ratio (CNR) comparison of Nd:YAG-based and FLOAT images. The regions of interest (ROIs) used to estimate the signal and noise are shown in red and yellow in b and c, respectively.

of low frequency signal components (Fig. 4b), the model-based reconstruction schemes offer an enhanced image quality and higher degree of image reconstruction accuracy (Fig. 4c) [46–48]. The presence of circular ring artifacts in cross-sectional finger images, caused by inherent electrical noise in the FLOAT system, can be effectively reduced by implementing a notch filtering in the signal domain (Fig. 4d). Statistically weighted model-based reconstruction [43] further mitigates the loss of resolution caused by acoustic heterogeneities and uneven light deposition across the finger. This resulted in reduced artifacts, clear delineation of skin boundaries and enhanced visualization of internal structures (Fig. 4e). Median filtering was subsequently applied for efficient smoothing of spiky noise and preserving sharp edges, while background signals were further suppressed outside the finger for final image contrast enhancement (Fig. 4f). The number of frames to be averaged (500) has been selected by considering the inevitable trade-off between image quality enhancement and acquisition time (Fig. 4g). While the images reconstructed with a single frame are dominated by noise, the skin boundary and internal large blood vessels are partially visible with only 10 averages. When the number of averaged frames was increased to 100, the skin boundary and almost all large vessels are easily discernible. With 500 averages, the background noise is reduced, revealing a clear skin boundary, large blood vessels and smaller microvascular structures. No significant changes in the image quality were noticed between 500 and 1000 averages.

Following the image enhancement, the skin boundary and several arbitrarily-oriented blood vessels are clearly visible in the reconstructed 2D cross-sectional image of the index finger obtained with FLOAT (Fig. 5a). The diameters of the resolvable blood vessels vary between 0.2 and 1 mm, i.e., major blood vessels along with arterioles and venules can be resolved. Anatomical structures can be detected up to a depth of ~ 3 mm, similar to what is achieved with laser-based OAT (Fig. 5b), demonstrating the potential of FLOAT for visualizing inflammatory diseases in peripheral joints. Peak-contrast-to-noise-ratio (PCNR) was then computed for the blood vessels located across different depths from the skin surface in the reconstructed images obtained with FLOAT (Fig. 5c) and with laser-based OAT (Fig. 5d). PCNR was defined as $20 * \log_{10}[(Peak\ Signal - Background)/Noise]$, where *Peak Signal* is the maximum signal amplitude within a single blood vessel at a particular depth, *Background* and *Noise* are the mean signal amplitude and standard deviation of noise in the ROI outside the finger region, respectively. Although the PCNR values for FLOAT were generally lower as compared to the laser-based OAT due to the significantly lower per-pulse energies, a similar signal decay with respect to depth was observed for both systems owing to the light intensity decay inside the tissue.

4. Discussion

Compared to pulsed laser systems, LEDs exhibit low peak power making them suboptimal for efficient optoacoustic signal generation, Yet, the FLOAT system introduced in this work takes advantage of close proximity of the LED arrays to the sample to generate sufficient energy density at the imaged sample. The LEDs offer a safe, cost-effective, lightweight and portable (reduced form factor) alternative for optoacoustic signal excitation compared to standard Nd:YAG lasers and PLDs. The price of the LEDs including driving electronics is approximately ~ 1–2 kUSD, significantly lower than conventional laser sources used for OAT whose cost typically exceeds 100 kUSD. This anticipates a wider dissemination of this technology, particularly in resource-limited settings.

Previously reported LED-based systems employed linear array transducers, which resulted in severe limited-view artifacts thus compromising image quality and quantification ability. FLOAT features instead an accurate tomographic imaging performance enabled with a custom-made full-ring circular ultrasound array transducer. Simultaneous full 360° panoramic light illumination is essential for an optimal imaging performance of the FLOAT system considering the low per-pulse optical energy. In this way, full cross-sectional imaging has been implemented with a relatively low number of averaged frames with the array kept in a static position. A much longer scan time is required for capturing the same FOV with commercially-available linear arrays that need to be rotated around the imaged object together with the illumination LED source [49]. This also helps minimizing blurring/motion artefacts thus potentially enabling real-time imaging if high-frame-rate acquisition is performed [50].

Similar to the Nd:YAG laser-based OAT system, FLOAT was capable of rendering high-resolution images from a tissue-mimicking phantom. Individual LEDs inherently suffer from low per-pulse energies of only a few μJ, which could be increased to a few 100 s of μJ by compact stacking. Sufficient SNR levels were achieved by 1) signal averaging, 2) notch filtering and 3) a weighted model-based iterative reconstruction

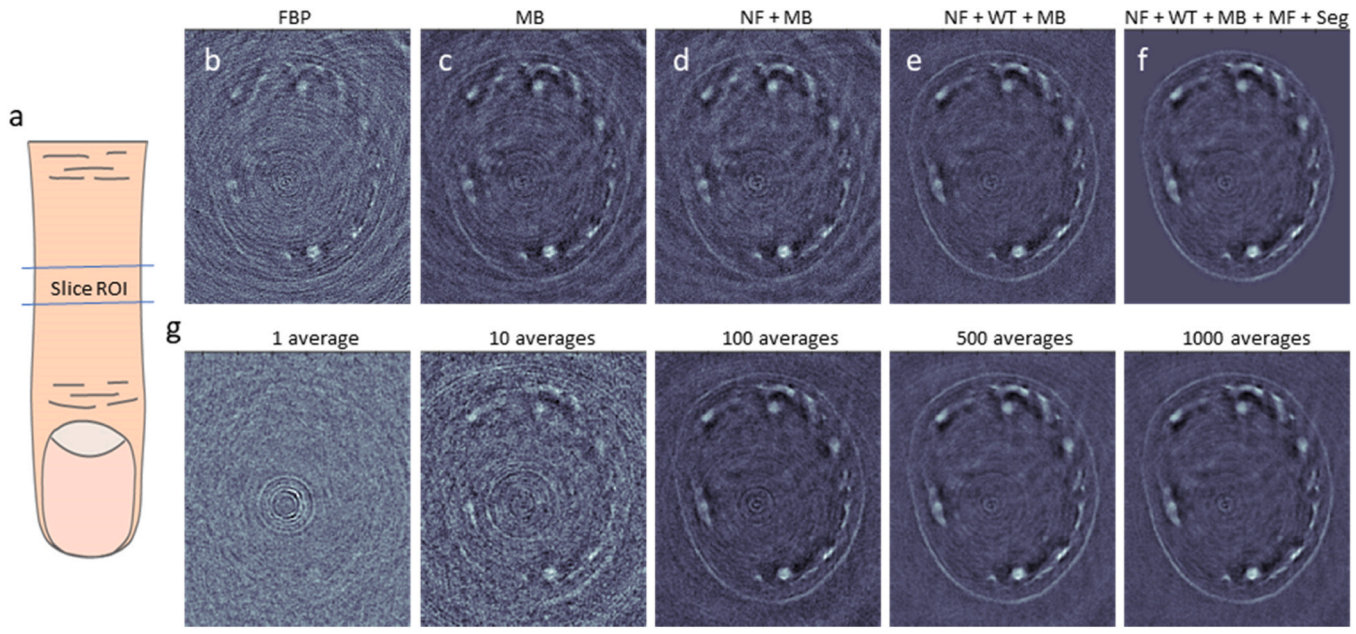

Fig. 4. Enhancement of FLOAT image contrast. a, Index finger schematic indicating the location of the imaging planes within the medial phalange. b, Cross-sectional image of index finger slice reconstructed using filtered back-projection algorithm. c, The corresponding model-based reconstruction. d, Notch-filtering in the signal domain reduces ring noise artifacts. e, Statistically weighted model-based algorithm mitigates artifacts cause by acoustic heterogeneities. f, Median filtering and background intensity suppression further enhances the image contrast. FBP: Filtered back-projection, MB: Model-based, NF: Notch filter, WT: weighted, MF: median filter, seg: segmented finger region. g, Difference in model-based reconstructed image contrast with different number of averaged frames.

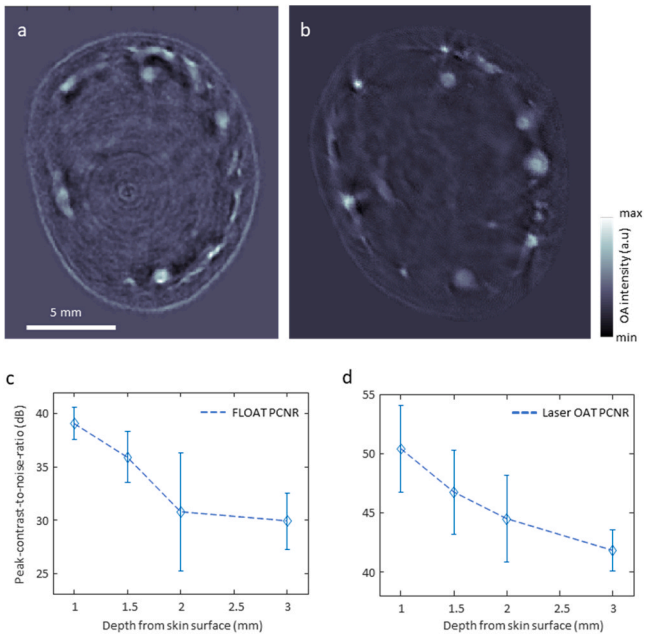

Fig. 5. In vivo human index finger imaging with FLOAT. a, Representative 2D cross sectional images obtained with FLOAT within the region of interest (ROI) marked in Fig. 4a. 500 consecutive frames were averaged for the reconstructions. b, The respective images acquired with the laser-based OAT system. c, Peak-contrast-to-noise-ratio (PCNR) computed as a function of depth from the skin surface for the FLOAT images. Four images were considered in calculating the mean and standard deviation/error bars. d, The respective PCNR for the laser-based OAT images.

[51]. The signal levels can be further enhanced with specifically designed transducer arrays enabling a more efficient distribution of stacked LED arrays. Dual- or multi-wavelength FLOAT can also be implemented by combining different types of LEDs. This implies either reducing the number of LEDs per wavelength or using a larger number of LEDs located at a larger distance from the tissue surface. Also, multi-wavelength imaging implies the design of a new LED electronic circuit to drive LEDs emitting light at different wavelengths in a consecutive manner.

We further demonstrated the feasibility of in vivo FLOAT. Vascular structures in the finger joint of a healthy volunteer were clearly visible with 500 signal averages. Note that the LEDs were operated at 50 Hz PRR, which resulted in a slow 0.1 Hz effective frame rate. By optimizing the thermal parameters, the PRR can potentially be increased to 1 kHz thus enabling 2 Hz effective frame rates without exceeding the laser safety limit of 40 mJ/cm^2 at the 850 nm illumination wavelength [52]. Multi-spectral imaging with LEDs operating at different wavelengths can potentially provide additional functional information related to blood oxygen saturation and contrast agent perfusion to the detriment of temporal resolution. This can greatly facilitate clinical translation e.g. to study synovial angiogenesis as a hallmark of early rheumatoid arthritis in human joints [53]. In addition, the circular-ring array transducer can be employed for transmission and reflection ultrasound imaging, thus providing highly complementary information on elastic and functional properties of the finger joints [54,55]. The limited SNR achieved with the current FLOAT system can potentially be improved by employing advanced reconstruction and processing methods. For example, ring artefacts appearing in the cross-sectional finger images are commonly attributed to electrical noise within the system and can potentially be reduced with deep-learning-based methods [56]. Other model-based least squares (LS) minimization techniques can be further employed to enhance the in vivo image quality and mitigate artefacts [57].

5. Conclusions

In summary, we have introduced a cost-effective, portable OAT system capable of tomographic acquisition with panoramic 360° light illumination using pulsed LEDs. The circular ultrasound array transducer provides optimal angular coverage to facilitate cross-sectional image acquisition and circumvent limited-view effects. FLOAT thus offers an affordable solution for optoacoustic imaging in various

preclinical and clinical settings, such as diagnosis and therapy monitoring in rheumatoid arthritis or small animal whole body imaging.

CRediT authorship contribution statement

Xiang Liu: Methodology, Investigation, Data curation, Software, Formal analysis, Visualization, Writing – original draft, Writing – review & editing. **Sandeep Kumar Kalva:** Conceptualization, Methodology, Investigation, Data curation, Software, Formal analysis, Visualization, Writing – original draft, Writing – review & editing. **Berkan Lafci:** Software. **Daniil Nozdriukhin:** Visualization. **Xosé Luís Deán-Ben:** Software, Resources, Formal analysis, Writing – review & editing. **Daniel Razansky:** Conceptualization, Methodology, Project administration, Resources, Supervision, Validation, Writing – review & editing.

Declaration of Competing Interest

The authors declare that they have no known competing financial interests or personal relationships that could have appeared to influence the work reported in this paper.

Data Availability

Data will be made available on request.

References

[1] S. Lei, et al., In vivo three-dimensional multispectral photoacoustic imaging of dual enzyme-driven cyclic cascade reaction for tumor catalytic therapy, Nat. Commun. 13 (1) (11 2022) 1298, https://doi.org/10.1038/s41467-022-29082-1.

[2] A.B.E. Attia, et al., A review of clinical photoacoustic imaging: current and future trends, Photoacoustics 16 (2019), 100144, https://doi.org/10.1016/j.pacs.2019.100144.

[3] Y. Yang, et al., Switching the NIR upconversion of nanoparticles for the orthogonal activation of photoacoustic imaging and phototherapy, Nat. Commun. 13 (1) (2022) 3149, https://doi.org/10.1038/s41467-022-30713-w.

[4] S. Manohar, M. Dantuma, Current and future trends in photoacoustic breast imaging, Photoacoustics 16 (2019), 100134, https://doi.org/10.1016/j.pacs.2019.04.004.

[5] A.P. Regensburger, et al., Detection of collagens by multispectral optoacoustic tomography as an imaging biomarker for Duchenne muscular dystrophy, Nat. Med. 25 (12) (2019) 1905, https://doi.org/10.1038/s41591-019-0669-y (in English).

[6] M.W. Schellenberg, H.K. Hunt, "and-held optoacoustic imaging: a review, Photoacoustics 11 (2018) 14–27, https://doi.org/10.1016/j.pacs.2018.07.001.

[7] J. Robin, et al., Hemodynamic response to sensory stimulation in mice: comparison between functional ultrasound and optoacoustic imaging, Neuroimage 237 (2021), 118111, https://doi.org/10.1016/j.neuroimage.2021.1181111 (in English).

[8] G. Balasundaram, et al., Noninvasive anatomical and functional imaging of orthotopic glioblastoma development and therapy using multispectral optoacoustic tomography, Transl. Oncol. 11 (5) (2018) 1251–1258, https://doi.org/10.1016/j.tranon.2018.07.001.

[9] V. Ntziachristos, D. Razansky, Molecular imaging by means of multispectral optoacoustic tomography (MSOT), Chem. Rev. 110 (5) (2010) 2783–2794, https://doi.org/10.1021/cr9002566.

[10] N.C. Deliolanis, et al., Deep-tissue reporter-gene imaging with fluorescence and optoacoustic tomography: a performance overview, Mol. Imaging Biol. 16 (5) (2014) 652–660, https://doi.org/10.1007/s11307-014-0728-1.

[11] K. Mishra, et al., Genetically encoded photo-switchable molecular sensors for optoacoustic and super-resolution imaging, Nat. Biotechnol. 40 (4) (2022) 598–605, https://doi.org/10.1038/s41587-021-01100-5.

[12] P. Vagenknecht, et al., Non-invasive imaging of tau-targeted probe uptake by whole brain multi-spectral optoacoustic tomography, Eur. J. Nucl. Med. Mol. Imaging 49 (7) (2022) 2137–2152, https://doi.org/10.1007/s00259-022-05708-w.

[13] M. Pramanik, L.V. Wang, Thermoacoustic and photoacoustic sensing of temperature, J. Biomed. Opt., vol. 14(no. 5), 2009, Artn 054024. ⟨https://doi.org/10.1117/1.3247155⟩. (in English).

[14] X. Gao, et al., A photoacoustic patch for three-dimensional imaging of hemoglobin and core temperature, Nat. Commun. 13 (1) (2022) 7757, https://doi.org/10.1038/s41467-022-35455-3.

[15] P.K. Upputuri, D. Das, M. Maheshwari, Y. Yaowen, M. Pramanik, Real-time monitoring of temperature using a pulsed laser-diode-based photoacoustic system, Opt. Lett. 45 (3) (2020) 718–721, https://doi.org/10.1364/OL.386173.

[16] A. Ozbek, X.L. Dean-Ben, D. Razansky, Optoacoustic imaging at kilohertz volumetric frame rates, Optica 5 (7) (2018) 857–863, https://doi.org/10.1364/Optica.5.000857 (in English).

[17] P. Rajendran, M. Pramanik, High frame rate (approximately 3 Hz) circular photoacoustic tomography using single-element ultrasound transducer aided with deep learning, J. Biomed. Opt. 27 (6) (2022), 066005, https://doi.org/10.1117/1.JBO.27.6.066005.

[18] A.A. Plumb, N.T. Huynh, J. Guggenheim, E. Zhang, P. Beard, Rapid volumetric photoacoustic tomographic imaging with a Fabry-Perot ultrasound sensor depicts peripheral arteries and microvascular vasomotor responses to thermal stimuli, Eur. Radiol. 28 (3) (2018) 1037–1045, https://doi.org/10.1007/s00330-017-5080-9.

[19] S.K. Kalva, X.L. Dean-Ben, D. Razansky, Single-sweep volumetric optoacoustic tomography of whole mice, Photon. Res., vol. 9(no. 6), 2021, pp. 899–908.

[20] S.K. Kalva, A. Sánchez-Iglesias, X.L. Deán-Ben, L.M. Liz-Marzán, D. Razansky, Rapid volumetric optoacoustic tracking of nanoparticle kinetics across murine organs, ACS Appl. Mater. Interfaces, vol. 14(no. 1), 2021, pp. 172–8.

[21] L. Li, et al., Single-impulse panoramic photoacoustic computed tomography of small-animal whole-body dynamics at high spatiotemporal resolution, Nat. Biomed. Eng. 1 (5) (2017) 0071, https://doi.org/10.1038/s41551-017-0071.

[22] S.K. Kalva, P.K. Upputuri, M. Pramanik, High-speed, low-cost, pulsed-laser-diode-based second-generation desktop photoacoustic tomography system, Opt. Lett. 44 (1) (2019) 81–84, https://doi.org/10.1364/OL.44.000081.

[23] M.H. Xu, L.H.V. Wang, Photoacoustic imaging in biomedicine, Rev. Sci. Instrum. 77 (4) (2006), 041101, https://doi.org/10.1063/1.2195024 (in English).

[24] S.K. Kalva, X.L. Dean-Ben, M. Reiss, D. Razansky, Whole-body imaging of mice in under 2 s with single-sweep volumetric optoacoustic tomography (sSVOT), Proc. Spie 11960 (2022), 1196005, https://doi.org/10.1117/12.2608652 (in English).

[25] J.S. Allen, P. Beard, Pulsed near-infrared laser diode excitation system for biomedical photoacoustic imaging, Opt. Lett. 31 (23) (2006) 3462–3464, https://doi.org/10.1364/OL.31.003462.

[26] S.K. Kalva, M. Pramanik, Photoacoustic Tomography with High Energy Pulsed Laser Diodes, SPIE Press, 2020.

[27] T.J. Allen, P.C. Beard, Light emitting diodes as an excitation source for biomedical photoacoustics, Proc. SPIE 8581 (2013) 85811F, https://doi.org/10.1117/12.2004471.

[28] X. Dai, H. Yang, H. Jiang, In vivo photoacoustic imaging of vasculature with a low-cost miniature light emitting diode excitation, Opt. Lett. 42 (7) (2017) 1456–1459.

[29] A. Hariri, J. Lemaster, J. Wang, A.S. Jeevarathinam, D.L. Chao, J.V. Jokerst, The characterization of an economic and portable LED-based photoacoustic imaging system to facilitate molecular imaging, Photoacoustics 9 (2018) 10–20, https://doi.org/10.1016/j.pacs.2017.11.001.

[30] M. Erfanzadeh, Q. Zhu, Photoacoustic imaging with low-cost sources; a review, Photoacoustics 14 (2019) 1–11.

[31] M.K.A. Singh, N. Sato, F. Ichihashi, Y. Sankai, Point-of-care functional and molecular imaging using LED-based photoacoustics, Tencon Ieee Reg. (2019) 109–113 ((in English).[Online]. Available: <Go to ISI>://WOS:000528677800022).

[32] W. Xia, et al., Handheld real-time LED-based photoacoustic and ultrasound imaging system for accurate visualization of clinical metal needles and superficial vasculature to guide minimally invasive procedures, Sensors 18 (5) (2018) 1394, https://doi.org/10.3390/s18051394.

[33] X.L. Dean-Ben, D. Razansky, Optoacoustic image formation approaches-a clinical perspective, Phys. Med. Biol. 64 (18) (2019) 18TR01, https://doi.org/10.1088/1361-6560/ab3522.

[34] C. Tian, C. Zhang, H. Zhang, D. Xie, Y. Jin, Spatial resolution in photoacoustic computed tomography, Rep. Prog. Phys. 84 (3) (2021), https://doi.org/10.1088/1361-6633/abdab9.

[35] K. Joseph Francis, Y.E. Boink, M. Dantuma, M.K. Ajith Singh, S. Manohar, W. Steenbergen, Tomographic imaging with an ultrasound and LED-based photoacoustic system, Biomed. Opt. Express 11 (4) (2020) 2152–2165, https://doi.org/10.1364/BOE.384548.

[36] E. Mercep, J.L. Herraiz, X.L. Dean-Ben, D. Razansky, Transmission-reflection optoacoustic ultrasound (TROPUS) computed tomography of small animals, Light Sci. Appl. 8 (2019) 18, https://doi.org/10.1038/s41377-019-0130-5.

[37] L. Li, et al., Single-impulse panoramic photoacoustic computed tomography of small-animal whole-body dynamics at high spatiotemporal resolution, Nat. Biomed. Eng. 1 (5) (2017), 0071, https://doi.org/10.1038/s41551-017-0071 (in English).

[38] M. Oeri, W. Bost, N. Sénégond, S. Tretbar, M. Fournelle, Hybrid photoacoustic/ultrasound tomograph for real-time finger imaging, Ultrasound Med. Biol. 43 (10) (2017) 2200–2212.

[39] Y. Liu, Y. Wang, Z. Yuan, Dual-modality imaging of the human finger joint systems by using combined multispectral photoacoustic computed tomography and ultrasound computed tomography, BioMed Res. Int. 2016 (2016).

[40] H. Guo, Q. Wang, W. Qi, X. Sun, B. Ke, L. Xi, Assessing the development and treatment of rheumatoid arthritis using multiparametric photoacoustic and ultrasound imaging, J. Biophotonics 12 (11) (2019), e201900127.

[41] B. Lafci , et al., Multimodal assessment of non-alcoholic fatty liver disease with transmission-reflection optoacoustic ultrasound, bioRxiv, 2022, p. 2022.08.16.504139.

[42] C. Willert, B. Stasicki, J. Klinner, S. Moessner, Pulsed operation of high-power light emitting diodes for imaging flow velocimetry, Meas. Sci. Technol. 21 (7) (2010), 075402, https://doi.org/10.1088/0957-0233/21/7/075402.

[43] X.L. Dean-Ben, R. Ma, D. Razansky, V. Ntziachristos, Statistical approach for optoacoustic image reconstruction in the presence of strong acoustic heterogeneities, IEEE Trans. Med. Imaging 30 (2) (2010) 401–408.

[44] S. Liu, et al., Validation of photoacoustic/ultrasound dual imaging in evaluating blood oxygen saturation, Biomed. Opt. Express 13 (10) (2022) 5551–5570, https://doi.org/10.1364/BOE.469747.

[45] S.L. Jacques, Optical properties of biological tissues: a review, Phys. Med. Biol. 58 (11) (2013) R37–61, https://doi.org/10.1088/0031-9155/58/11/R37.

[46] L. Ding, D. Razansky, X.L. Dean-Ben, Model-based reconstruction of large three-dimensional optoacoustic datasets, IEEE Trans. Med. Imaging 39 (9) (2020) 2931–2940.
[47] W. Li, et al., Broadband model-based optoacoustic mesoscopy enables deep-tissue imaging beyond the acoustic diffraction limit, Laser Photonics Rev. 16 (5) (2022) 2100381.
[48] X.L. Deán-Ben, D. Razansky, A practical guide for model-based reconstruction in optoacoustic imaging, Front. Phys. 10 (2022) 1057.
[49] K.J. Francis, Y.E. Boink, M. Dantuma, M.K.A. Singh, S. Manohar, W. Steenbergen, Tomographic imaging with an ultrasound and LED-based photoacoustic system, Biomed. Opt. Express 11 (4) (2020) 2152–2165.
[50] C. Ozsoy, A. Ozbek, M. Reiss, X.L. Dean-Ben, D. Razansky, Ultrafast four-dimensional imaging of cardiac mechanical wave propagation with sparse optoacoustic sensing, Proc. Natl. Acad. Sci. USA 118 (45) (2021), https://doi.org/10.1073/pnas.2103979118.
[51] X.L. Deán-Ben, D. Razansky, V. Ntziachristos, Statistical weighting of model-based optoacoustic reconstruction for minimizing artefacts caused by strong acoustic mismatch, in: Photons Plus Ultrasound: Imaging and Sensing 2011, 2011, vol. 7899, SPIE, 2011, pp. 607–14.
[52] I. American National Standards, A. Laser Institute of, American National Standard for Safe Use of Lasers (ANSI Z136.1-2007), The Institute, Orlando, FL, 2007, pp. xiii, 249 p.: ill, (in English).
[53] D.A. Walsh, Angiogenesis and arthritis, Rheumatology 38 (2) (1999) 103–112, https://doi.org/10.1093/rheumatology/38.2.103.
[54] B. Lafci, E. Merčep, J.L. Herraiz, X.L. Deán-Ben, D. Razansky, Noninvasive multiparametric characterization of mammary tumors with transmission-reflection optoacoustic ultrasound, Neoplasia 22 (12) (2020) 770–777.
[55] E. Merčep, J.L. Herraiz, X.L. Deán-Ben, D. Razansky, Transmission–reflection optoacoustic ultrasound (TROPUS) computed tomography of small animals, Light: Sci. Appl., vol. 8(no. 1), 2019, p. 18, 2019/01/30. ⟨https://doi.org/10.1038/s41377-019-0130-5⟩.
[56] C. Dehner, I. Olefir, K.B. Chowdhury, D. Justel, V. Ntziachristos, Deep-learning-based electrical noise removal enables high spectral optoacoustic contrast in deep tissue, IEEE Trans. Med. Imaging 41 (11) (2022) 3182–3193, https://doi.org/10.1109/TMI.2022.3180115.
[57] X.L. Dean-Ben, D. Razansky, A practical guide for model-based reconstruction in optoacoustic imaging, Front. Phys., vol. 10, 2022. ARTN 1028258. ⟨https://doi.org/10.3389/fphy.2022.1028258⟩. (in English).

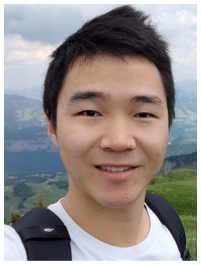

Xiang Liu has been pursuing his Ph.D. at ETH Zurich and University of Zurich under the supervision of Prof. Daniel Razansky at the Institute of Pharmacology and Toxicology and the Institute for Biomedical Engineering since 2021. He obtained his B.Sc degree from Tongji University in 2018 and completed his M.Sc in Mechatronics at the Karlsruhe Institute of Technology in 2021. His primary research focus lies in developing low-cost, compact, and portable optoacoustic systems, encompassing both mechanical and electrical engineering design aspects.

Sandeep Kumar Kalva is working as a postdoctoral fellow in Prof. Daniel Razansky's group at the Institute of Pharmacology and Toxicology and the Institute for Biomedical Engineering, University of Zurich and ETH Zurich, Switzerland since November, 2019. Previously, he earned Ph.D. in Biomedical Engineering from the Nanyang Technological University, Singapore. His research is focused on development and application of new optoacoustic imaging systems for various biomedical applications in cancer theranostics. He has published 29 peer-reviewed journal articles, 12 conference proceedings and 1 book chapter.

Berkan Lafci received the B.Sc. degree in electrical and electronics engineering from Bogazici University, Turkey, in 2016, the M.Sc. degree in biomedical computing from the Technical University of Munich, Germany, in 2018, and the Ph.D. degree in information technology and electrical engineering from ETH Zurich in 2023. He is currently a postdoc at the University of Zurich focusing on the development of volumetric reconstruction and segmentation algorithms. His general research interests also include multimodal medical image processing algorithms using deep learning-based methods.

Daniil Nozdriukhin received his B.Sc degree in physics from Peter the Great St. Petersburg Polytechnic University in 2018 and finished his M.Sc at Skoltech, Moscow at the Center for Photonics and Quantum Materials in 2020. He is currently pursuing PhD studies at ETH Zurich and University of Zurich. His main research areas are contrast agents for optoacoustics, layer-by-layer microparticle assembly and their characterization.

Xosé Luís Deán-Ben has been working in the field of optoacoustic (photoacoustic) imaging since 2010. He currently serves as a senior scientist and group leader at the Institute for Biomedical Engineering and Institute of Pharmacology and Toxicology, University of Zurich and ETH Zurich. Previously, he received post-doctoral training at the Institute of Biological and Medical Imaging, Helmholtz Zentrum Munich. He contributed both to the development of new optoacoustic systems and processing algorithms as well as to the demonstration of new bio-medical applications in cancer research, cardiovascular biology and neuroscience. He has co-authored more than 150 papers in peer-reviewed journals on these topics.

Daniel Razansky holds the Chair of Biomedical Imaging with double appointment at the Faculty of Medicine, University of Zurich and Department of Information Technology and Electrical Engineering, ETH Zurich. He earned Ph.D. in Biomedical Engineering and M.Sc. in Electrical Engineering from the Technion - Israel Institute of Technology and completed post-doctoral training in bio-optics at the Harvard Medical School. Between 2007 and 2018 he was the Director of Multi-Scale Functional and Molecular Imaging Lab and Professor of Molecular Imaging Engineering at the Technical University of Munich and Helmholtz Center Munich. His Lab pioneered and commercialized a number of imaging technologies, among them the multi-spectral optoacoustic tomography and hybrid optoacoustic ultrasound imaging. He has authored over 300 peer-review journal articles and holds 15 patented inventions in bio-imaging and sensing. He is the Founding Editor of Photoacoustics journal and serves on Editorial Boards of a number of journals published by Springer Nature, Elsevier, IEEE and AAPM. He is also an elected Fellow of the IEEE, Optica and SPIE.